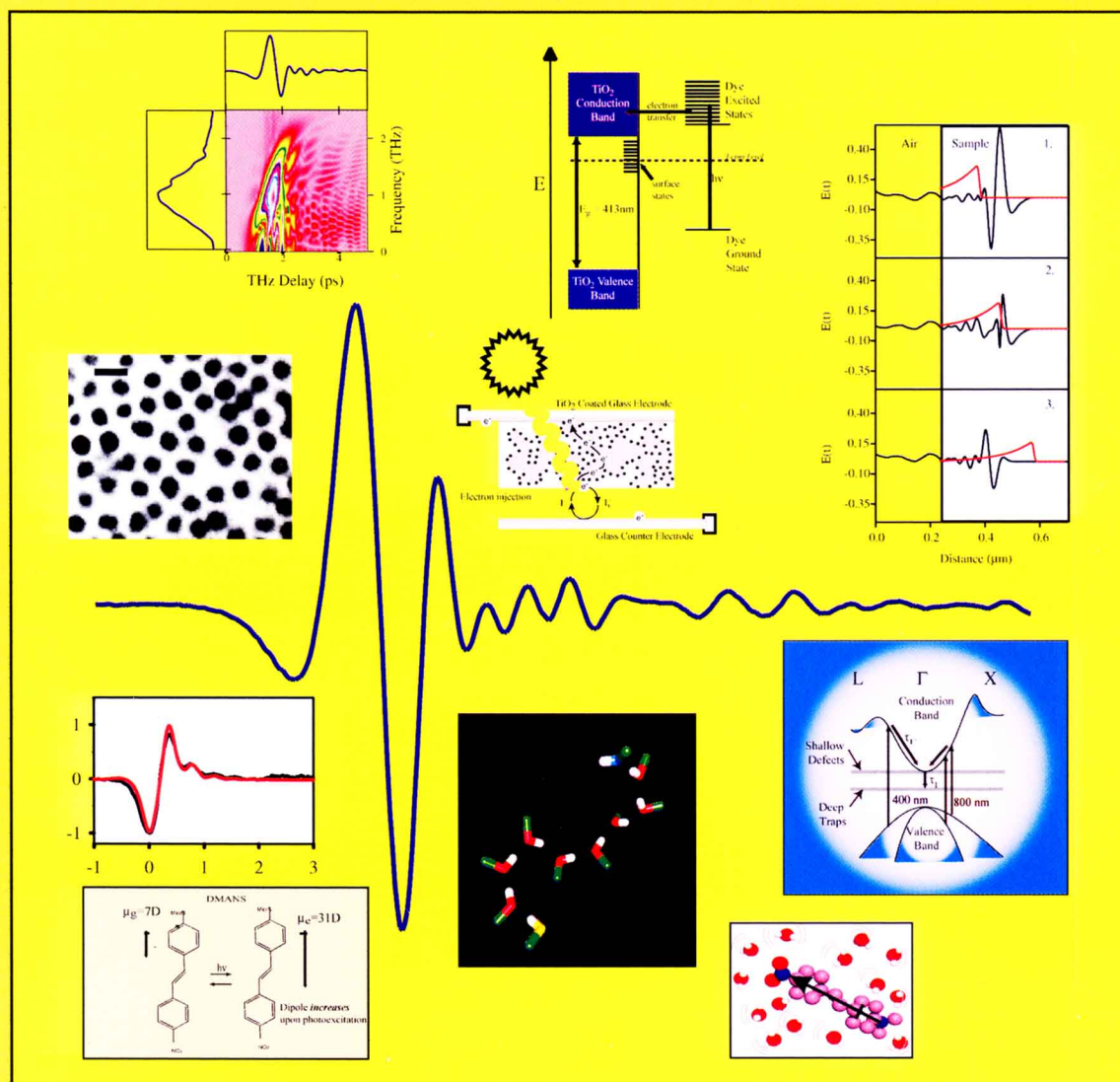


VOLUME 106  
JULY 25, 2002  
NUMBER 29

<http://pubs.acs.org/JPCB>

# THE JOURNAL OF PHYSICAL CHEMISTRY

# B



Terahertz Spectroscopy  
Provides New Insights  
into Many Different  
Dynamical and Nanoscale  
Systems  
(see page 5A)

CONDENSED MATTER, MATERIALS, SURFACES, INTERFACES, & BIOPHYSICAL CHEMISTRY

PUBLISHED WEEKLY BY THE AMERICAN CHEMICAL SOCIETY



## FEATURE ARTICLE

## Terahertz Spectroscopy

Matthew C. Beard, Gordon M. Turner, and Charles A. Schmuttenmaer\*

Department of Chemistry, Yale University, 225 Prospect Street, P.O. Box 208107, New Haven, Connecticut 06520-8107

Received: March 1, 2002; In Final Form: May 8, 2002

Terahertz spectroscopy emerged about 13 years ago with the demonstration that nearly single-cycle pulses of far-infrared radiation could be generated, propagated through free space, and subsequently detected in the time-domain. Since then, THz spectroscopy has found widespread applicability with studies ranging from condensed matter physics to gas-phase spectroscopy to biomedical imaging. In this article, the properties and applications of THz spectroscopy are described in the context of work being done in the Schmuttenmaer labs at Yale University. In particular, it is shown that an optical pump–THz probe configuration can elucidate phenomena such as the response of low-frequency collective solvent modes in liquids, and transient photoconductivity in a variety of semiconductor systems, such as bulk GaAs, low-temperature grown GaAs, nanocrystalline colloidal TiO<sub>2</sub>, and CdSe quantum dots. In addition, recent experiments measuring charge transfer in a very direct manner are discussed.

## I. Introduction

What is terahertz (THz) spectroscopy? As a working definition, THz spectroscopy covers the spectral range from about 3 cm<sup>-1</sup> to about 600 cm<sup>-1</sup>, also known as the far-infrared (far-IR) region of the spectrum. This implies frequencies on the order of ~0.1 to 20 THz since 1 THz is equivalent to 33.33 cm<sup>-1</sup>. In a more literal sense, any work in the frequency range from 0.1 to 100 THz can rightfully be regarded as THz spectroscopy. However, in light of developments over the last 13 years, the connotations of this terminology, especially in the context of “THz time domain spectroscopy”, or “time-resolved THz spectroscopy”, are that it implies generation and detection of THz pulses in a synchronous, coherent manner using visible or near-IR laser pulses. This is the intended meaning of “THz Spectroscopy” throughout this article.

The fact that THz pulses are created and detected using short-pulsed visible lasers with pulse widths ranging from ~100 fs down to ~10 fs adds a new element that is not present in conventional far-IR studies: It is now possible to carry out *time-resolved* far-IR studies with subpicosecond temporal resolution. In contrast, other sources of far-IR radiation such as arc lamps or globars are continuous, and pulsed sources such as free electron lasers or synchrotrons produce far-IR pulses with ~3 ps duration or greater. The majority of the work presented in this article exploits this time-resolved aspect of THz spectroscopy. An additional advantage of THz spectroscopy is that the transient electric field itself is measured, not simply its intensity, and this determines the amplitude and phase of each of the spectral components that make up the pulse. The amplitude and phase are directly related to the absorption coefficient and index of refraction of the sample, and thus the complex-valued permittivity of the sample is obtained without having to carry out a Kramers–Kronig analysis. While there exist methods for determining the index of refraction when using conventional far-IR sources and detectors, it is noted that the great majority

of the far-IR results reported in the literature present the frequency-dependent absorption coefficient, but not the refractive index. In this respect, THz spectroscopy provides a convenient method for determining the complex permittivity, even for studies that are not time-resolved.

**A. History.** THz spectroscopy grew out of efforts to generate and detect ultrashort electrical transients as they propagated down a transmission line. Research groups led by Dan Grischkowsky (then at IBM Watson Research Center), David Auston (then at Columbia University, Department of Physics), and Martin Nuss (then at Bell Labs) were all active in this area. As understood from Maxwell's equations, a time-varying electric current will radiate an electromagnetic (EM) pulse. Thus, it was realized that these transmission lines were also radiating short bursts of EM radiation. A radical change occurred in 1988/1989 when reports were published wherein these radiated pulses were propagated through free space from a generator to a detector.<sup>1,2</sup> At this point, one could now envision using these elements as a far-IR light source and detector pair, and one could place a sample between the two of them. THz spectroscopy was born.

Since then, on the order of 60 research groups worldwide have embraced THz spectroscopy in one form or another. Some utilize the fact that it is a high-brightness source in the far-IR, some utilize the ease of determining both the absorption coefficient and refractive index, some have carried out imaging studies, and a few have pursued time-resolved studies. For reasons unknown, THz spectroscopy is only now making inroads into the field of physical chemistry. While the apparatus is not trivial, it is no more difficult to build and operate than most research-level spectroscopic experiments. However, in fairness it should be noted that while it is relatively easy to construct an apparatus to generate and detect THz pulses, it is significantly more difficult to do so reproducibly and in a manner in which quantitative information about the sample is obtained.

The history of far-IR spectroscopy in general goes back much further, and there are strong ties to the microwave and mm-

wave communities.<sup>3</sup> The earliest work typically employed arc lamp sources and bolometric detection. However, the power delivered by an arc lamp falls off precipitously at long wavelengths. When weak sources are being detected, there can be interference from the laboratory surroundings due to blackbody radiation. There have been many improvements to this type of technology over the years, and modern sources now include fixed frequency far-IR lasers, tunable sources based on mixing a fixed frequency laser with output from a tunable microwave generator, or mixing together two IR or near-IR lasers. High-brightness synchrotron sources and free electron lasers are used in far-IR studies with increasing regularity. Exquisitely sensitive hot electron bolometers, and superconducting hot electron bolometers, developed primarily for far-IR astronomy, have been fabricated. Note that all of these techniques are inherently continuous wave (cw), and are of limited utility for time-resolved studies. Exceptions are synchrotrons and free electron lasers, but even those have pulse widths on the order of 3–10 ps, which makes it difficult to obtain dynamical information on a sub-picosecond time scale.

The allure of THz spectroscopy can now be understood: (1) it is a tabletop experiment with brightness equal to or exceeding synchrotron sources (at long wavelengths), (2) Coherent detection allows pulses below the blackbody radiation level to be measured without the use of specialized detectors, and (3) time-resolved studies are now possible in the far-IR region of the spectrum.

**B. Other THz Work.** This article will focus on the studies underway in the Schmuttenmaer labs at Yale University, but the type of work being done in the field in general should be discussed briefly. As previously mentioned, there are about 60 research groups worldwide using THz spectroscopy in one form or another, and there simply is not enough space to summarize each of these efforts. Instead, we will merely present a sampling that is hoped to be of interest to physical chemists. These topics include: (1) gas-phase spectroscopy, (2) THz imaging studies, (3) three-dimensional imaging, (4) polar and nonpolar liquids, (5) biological media, (6) solid-state materials, (7) THz sources and detectors.

*i. Gas-Phase Spectroscopy.* There has been some very innovative gas-phase spectroscopy from Grischkowsky, Harde, Cheville, and their co-workers. For example, they have investigated the tunneling-inversion in methyl halides such as CH<sub>3</sub>Cl.<sup>4</sup> The concept of methyl halides undergoing tunneling-inversion seems hard to believe initially, but it actually occurs. They have also measured rotational transitions of water in flames. It would be impossible to use a standard intensity-based detector to observe the far-IR absorption spectrum of a molecule in the midst of a 1300–1500 K flame.<sup>5,6</sup>

*ii. T-ray Imaging.* THz imaging of plant and animal material debuted in 1995.<sup>7,8</sup> In this context, THz spectroscopy is often referred to as T-ray imaging.<sup>9,10</sup> It has been possible to image biological samples, with especially striking results of specimens that have a high contrast of aqueous and nonaqueous regions. In addition, because far-IR radiation passes through many plastics that visible and IR radiation cannot, it is possible, for example, to image the layout inside integrated chip packages using T-rays.<sup>8</sup> There have also been some very impressive studies by Nuss and Mittleman with regard to THz imaging of semiconductor wafers. They demonstrated that it is possible to map out the doping density in 2 in. diameter *n*- and *p*-type wafers with sub-millimeter resolution.<sup>11</sup> Images are often obtained by raster-scanning the sample through the focused THz beam. It is also possible to collect a two-dimensional (2D) image

using a CCD camera as a detector, which allows very high data acquisition rates.<sup>12</sup>

*iii. Three-Dimensional Imaging.* THz ranging and tomography, wherein the echo or return of a pulse reflected off an object is captured and analyzed or the transmitted beam is analyzed as the sample is rotated, are still in their infancy, but the work done by Cheville and Grischkowsky,<sup>13,14</sup> and Nuss and Mittleman,<sup>9,15,16</sup> have shown that there is great potential. This type of study exploits the time-resolved nature of THz spectroscopy, but not in a pump–probe configuration. For example, the various layers comprising a computer floppy disk were revealed by deconvolving the input THz waveform from the reflected waveform.<sup>9</sup> The development of three-dimensional (3D) imaging techniques will be absolutely essential for the use of THz imaging in biological and nonbiological media, which are two areas of much recent activity.

*iv. Polar and Nonpolar Liquids.* There has been a fair amount of non-time-resolved work directed toward studies of polar, nonpolar, and mixtures of liquids primarily from the Schmuttenmaer and Keiding laboratories.<sup>17–26</sup> Collective, low-frequency, intermolecular modes of liquids occur in the far-IR region of the spectrum. Studying liquids with THz time-domain spectroscopy determines the real and imaginary components of the permittivity, which is then related to the intermolecular dynamics. For example, it is possible to quantify the Debye relaxation time as a function of temperature or composition (in the case of a binary mixture). These topics will be covered in more detail in section III. Keiding and co-workers often utilize a reflection setup,<sup>20,21,27</sup> rather than transmission when studying highly absorbing samples. Conversely, weak to moderately absorbing materials are typically best studied in transmission. In either case, the fact that the THz pulse amplitude is measured allows the complex-valued reflection and/or transmission coefficients to be determined unambiguously.

There has been a small amount of time-resolved work involving liquids ranging from solvent reorientation dynamics<sup>28–30</sup> to electron solvation.<sup>31</sup> Furthermore, a recent study by Cook and Hochstrasser displayed how THz spectroscopy can be used in a nonlinear fashion to investigate liquid dynamics.<sup>32</sup> Due to symmetry considerations, isotropic bulk liquids are not capable of second harmonic generation (SHG). However, Cook and Hochstrasser utilized the electric field of a THz pulse to induce a transient anisotropy in two polar liquids, which was monitored and understood through the process of SHG of a visible pulse arriving during and after application of the THz pulse.

*v. Biological Media.* The use of THz spectroscopy to study systems of biological significance seems quite reasonable, given that proteins have low-frequency motions that fall in the far-IR region of the spectrum. Oddly enough, there have only been a few THz investigations.<sup>33</sup> For example, Markelz and Heilweil reported the spectra of DNA, lysozyme, and collagen,<sup>34</sup> Jepsen et al. measured the far-IR spectrum of retinal,<sup>35</sup> and Brucherseifer et al. have measured the difference between hybridized and nonhybridized DNA.<sup>36</sup> In these early stages, one of the primary interests has been reproducibility and finding optimal sample conditions. One would expect this area of THz spectroscopy to grow rapidly soon.

*vi. Solid-State Materials.* THz spectroscopy has probably been used most extensively to study solids. Typically semiconductors are characterized, but conducting polymers,<sup>37</sup> insulators,<sup>28,38–40</sup> and superconductors<sup>41–43</sup> have also been studied. Electronic processes, such as conductivity<sup>44,45</sup> and transient conductivity,<sup>46–51</sup> as well as lattice modes (phonons),<sup>52–54</sup> have been investigated. THz spectroscopy is a natural fit for this type of work because

scattering events of carriers in semiconductors, either doped or photoexcited, tend to be on time scales of tens to hundreds of femtoseconds. This leads to distinct variations in the real and imaginary components of the complex conductivity in the THz region of the spectrum. Phonon modes in solids are often found in the range of several THz to tens of THz, which overlaps nicely with the spectral region covered by THz spectroscopy.

*vii. THz Sources and Detectors.* Some of the most important work in THz spectroscopy involving semiconductors has been directed toward novel THz sources and detectors. If it were not for the sources and detectors, then nothing else would be accomplished: it is quite difficult to drive a nail without using a hammer. Much credit goes to Auston, Grischkowsky, Nuss, and Zhang, and all of their co-workers. In broad terms, and with many exceptions, Grischkowsky et al. have concentrated on photoconductive transmitters and receivers employing unamplified lasers, and in particular silicon-on-sapphire technology,<sup>55</sup> whereas Zhang et al. have concentrated on high pulse energy applications requiring transmitters based on optical rectification and receivers based on free-space electro optic sampling.<sup>56</sup> Nuss et al. have optimized electrode shapes and techniques for near-field imaging.<sup>9,57</sup> In addition, there have been exciting developments from both the Zhang and Leitenstorfer groups in an effort to generate even higher frequencies and larger bandwidths.<sup>58,59</sup> Certainly, other workers have contributed to source development, but a comprehensive account of these activities would require a full article in itself.

A related issue is the analysis of THz pulses emitted from various materials to learn about the carrier dynamics of the materials themselves.<sup>60–62</sup> This type of study has been carried out for quantum wells,<sup>63,64</sup> for GaAs under different applied bias voltages,<sup>64–66</sup> at a variety of temperatures,<sup>67</sup> and as a function of magnetic field.<sup>68</sup> As will be discussed in section IV.B, we have used THz pulse generation to probe intramolecular charge transfer in solution.<sup>69,70</sup>

**C. Scope of This Article.** This article describes recent and current work involving THz spectroscopy taking place in the Schmuttenmaer labs at Yale University. The Experimental Section presents two types of THz spectrometers: one based on an unamplified laser that is used for nontime-resolved studies, and the other based on an amplified laser system that is used for time-resolved studies. The Experimental Section will also introduce some issues related to proper workup of the data, and a numerical propagation method that we find very useful when simulating the experiments. Section III briefly describes nontime-resolved studies of liquids and binary liquid mixtures as well as molecular dynamics (MD) simulations. Section IV is concerned with time-resolved THz spectroscopy (TRTS). Efforts to probe the low-frequency collective solvation response in liquids are described, including our studies of rapid electron transfer as studied by measuring the THz pulse emitted by a sample that is coherently photoexcited. Then, transient photoconductivity in GaAs, low-temperature grown GaAs (LT-GaAs), and colloidal TiO<sub>2</sub> are reported, followed by the transient “photoconductivity” in semiconductor quantum dots. Section V presents ideas for future studies, and Section VI concludes the article.

## II. Experimental Considerations

**A. Unamplified System.** Figure 1 is a schematic diagram of our spectrometer used for THz time-domain spectroscopy (THz-TDS). Note, these are not *time-resolved* measurements, the name merely implies that the measurements are made in the time-domain, and then Fourier transformed into the frequency

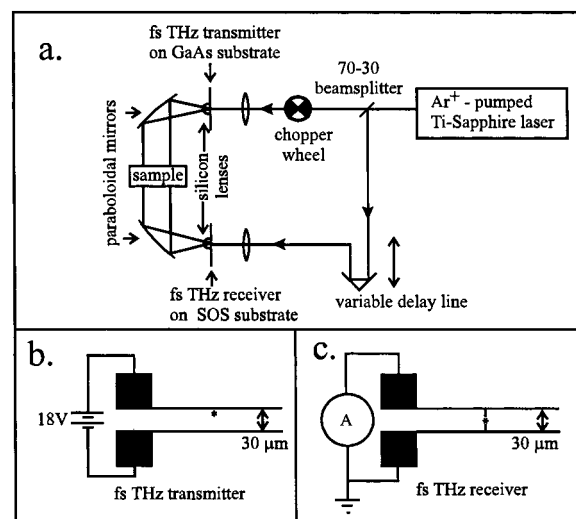


**Figure 1.** Schematic diagram of THz-TDS spectrometer. A femtosecond THz pulse is generated at the transmitter when it is illuminated by a visible fs pulse from the Ti-sapphire laser. After collimation by the lens and paraboloidal mirror, the femtosecond THz pulse passes through the sample and is refocused at the receiver. The receiver is gated synchronously by a portion of the beam split-off from the visible pulse, so that the current flow at the receiver will map out the time-dependent electric field of the femtosecond THz pulse as the variable delay is adjusted. Parts b and c: Schematic diagram of femtosecond THz transmitter and receiver geometries. The asterisk represents the site at which the visible laser is focused. Reprinted with permission from ref 18. Copyright 1996 American Chemical Society.

domain. The design of this spectrometer is based on refs 1 and 55, and is a standard configuration.

Photoconductive antennas are used for the generation and detection of THz pulses. The THz pulses are generated at the transmitter when a 100 fs duration pulse of 800 nm light excites carriers into the conduction band of the GaAs substrate. The transmission line provides a bias voltage of  $\sim 5000$  V/cm which accelerates the newly formed carriers. This acceleration of charge radiates an EM pulse. The width of the radiated pulse depends on the duration of the visible pulse as well as the thickness of the GaAs wafer. GaAs has strong longitudinal optical (LO) phonon absorption near 9 THz, and the tail of this absorption attenuates high-frequency components of the THz pulse, thereby limiting how short it can be. Thinner wafers absorb less strongly, but are extremely fragile.

The receiver consists of a transmission line bridged by an antenna with a gap in the center. Its operation is similar to the transmitter, except that rather than applying a dc bias voltage, the transient THz field itself provides the bias voltage. If the gap is gated by the visible pulse when there is a large THz field, carriers will move from one side of the antenna to the other. The material used for the receiver has a very short carrier lifetime. Therefore, the electrons flow for roughly 100 fs, and after the THz pulse has passed and there is no longer a bias voltage, the electrons cannot travel back because the carriers have relaxed. Instead, charge flows from ground through the picoammeter in proportion to the amplitude of the THz field at the moment when the visible pulse gated the receiver. The full waveform is mapped out by stepping the variable delay line incrementally. The sign of the field is determined in addition to its magnitude. Optimization of this type of spectrometer has been discussed by many authors.

**B. Amplified System.** The amplified system is based on a regeneratively amplified Ti:Sapphire laser providing pulses at a 1 kHz repetition rate, with 100 fs pulse duration, and 1 mJ/

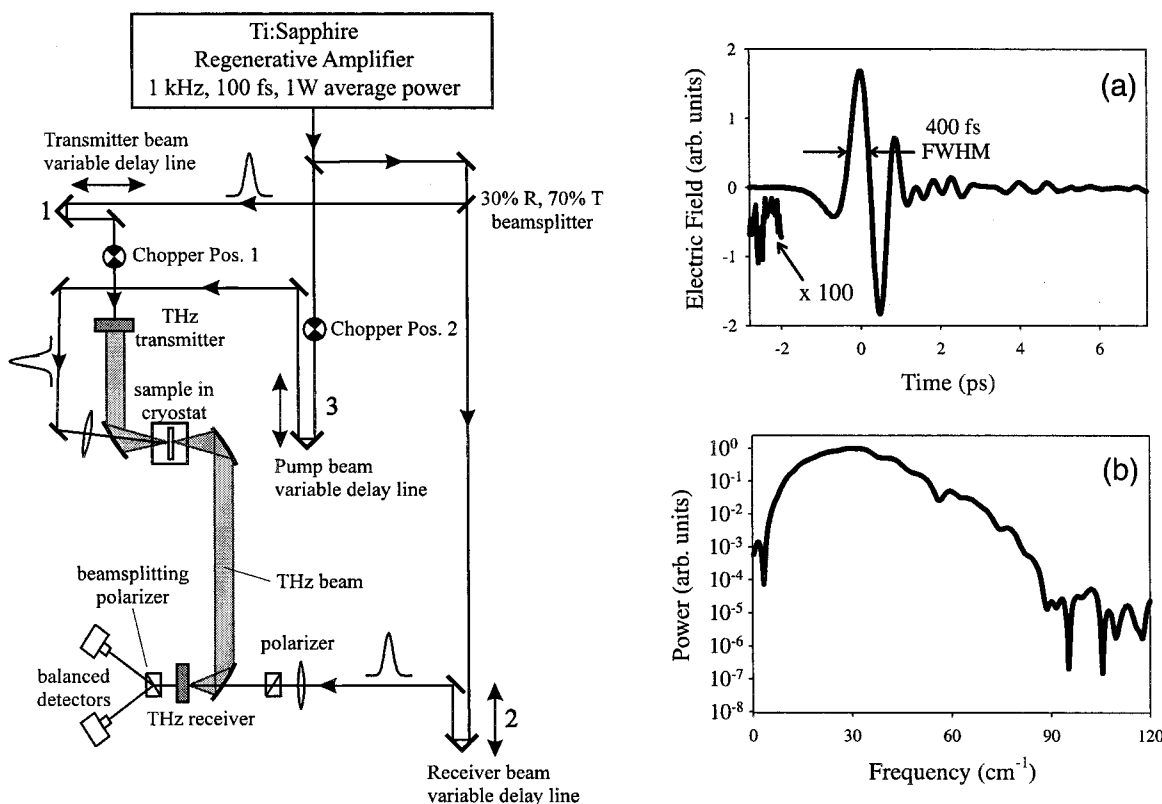


**Figure 2.** Experimental apparatus used to collect TRTS spectra. A reference scan is collected with the chopper in position 1, and a photoexcited difference scan is collected with the chopper in position 2. The THz amplitude is monitored by changing the relative delay of table 1 or table 2 depending on the type of experiment being performed (see text for more detail). Delay table 3 is used to change the relative delay of the pump beam. Plot a shows a typical time-domain THz transient of about 400 fs duration (fwhm) and S/N of roughly 1000:1. Plot b shows the power spectrum of the THz pulse. Reprinted with permission from ref 49. Copyright 2000 American Physical Society.

pulse energy, at 800 nm wavelength (Spectra Physics), and is shown schematically in Figure 2. The time-domain THz amplitude and frequency domain power spectrum are also shown in Figure 2.

Nonresonant optical rectification of the visible pulse in a 1 mm thick  $\langle 110 \rangle$  ZnTe crystal (II-IV, Inc.) is used for pulse generation.<sup>71,72</sup> Optical rectification is the difference frequency analogue of second harmonic generation. That is, when light interacts with a nonlinear medium and wave mixing between two frequencies  $\omega_1$  and  $\omega_2$  occurs, the result is sum-frequency generation,  $\omega_1 + \omega_2$ , and difference-frequency generation,  $\omega_1 - \omega_2$ . In the case where  $\omega_1 = \omega_2$ , one generates the same amplitude of second harmonic and dc. Because the visible pulses have a duration of  $\sim 100$  fs, a THz pulse is generated rather than a constant dc level.

The THz radiation is detected by free-space electrooptic sampling (FSEOS) in another 0.5 mm thick  $\langle 110 \rangle$  ZnTe crystal.<sup>56,72–74</sup> FSEOS is based on the Pockels effect in which an applied voltage causes the detector crystal to become birefringent. Thus, if the visible sampling pulse travels through the crystal at the same time as one point in the THz pulse, then its polarization will be rotated. The magnitude of rotation is proportional to the magnitude of the THz field, and the direction of rotation is proportional to the sign of the field. In this manner, the entire pulse amplitude is mapped out. The signal is collected with a lock-in amplifier (Stanford Research Systems SR830) phase-locked to an optical chopper (DigiRad C-980), which modulates either the THz generation arm or the pump beam depending on the type of experiment being performed. The THz beam path from the transmitter to the receiver is enclosed and purged with dry nitrogen to minimize THz absorption by water vapor.

A collimated 2 mm diameter visible beam with energy of 230  $\mu\text{J}/\text{pulse}$  is typically used for THz generation, and a focused 200  $\mu\text{m}$  diameter visible beam of 4.5 nJ/pulse is used for THz detection. The pump beam can be frequency-doubled to 400 nm in a 1 mm thick  $\beta\text{-BaB}_2\text{O}_4$  (BBO) crystal (Quantum Technologies) if needed. The pump beam energy ranges from 1 to 100  $\mu\text{J}/\text{pulse}$ . The pump beam spot size (the diameter at which the intensity of a Gaussian beam falls to  $1/e^2$  of its value at the beam center) must be significantly larger than that of the THz probe beam, which is between 2 and 4 mm. The two beams are collinearly propagated to minimize temporal smearing. Previous studies on GaAs have shown that if the diameter of the spot size is too small compared to that of the THz beam, then the far-IR spectrum may be skewed to higher frequencies.<sup>49</sup>

There are three different methods of data collection employed in TRTS experiments, as described in detail in our earlier work.<sup>49,50,75</sup> To summarize, we can either scan the probe delay line, pump delay line, or both, resulting in one-dimensional (1D) probe, 1D pump, or 2D data sets. The 1D probe experiments are carried out by setting delay line no. 3 at a position to photoexcite the sample well before the arrival of the THz pulse and scanning delay line no. 2 to map out the THz pulse. This yields the frequency-dependent optical constants of the sample, and in the case of semiconductors can be directly related to the photoconductivity of the sample without the use of any models or approximations.

One-dimensional pump experiments are performed by fixing delay line no. 2 at the position corresponding to the highest point on the THz waveform, and scanning the pump delay line no. 3 to vary the arrival time of the pump pulse relative to the THz probe pulse. This yields information about the onset and decay of photoconductivity in semiconductors. These experi-

ments, however, can be easily misinterpreted because changes in *either* the THz absorption coefficient or index of refraction can manifest themselves as what appear to be transient absorptions or bleaches in the 1D pump experiments. One-dimensional pump scans are also prone to variations resulting from slight differences in the precise positioning of the probe delay line on the THz waveform. However, 1D pump scans are very useful for estimating the overall signal-to-noise ratio, and for ascertaining the time scale(s) of the dynamics.

In a 2D experiment, both delay lines are scanned synchronously. This allows the full THz pulse to be measured in a fashion such that each point in the THz pulse is sampling the medium at the same amount of time after (or before) photoexcitation. It is therefore advisable to analyze the results from both types of 1D experiments with the aid of a 2D experiment, which is the only way to unambiguously measure the complete dynamics of the system. When probing the sample within the first few hundred femtoseconds after photoexcitation, one must be careful that the detector response does not interfere with the measured spectrum. As described previously,<sup>49</sup> this is only a problem when the response of the sample is faster than that of the detector.

**C. Thin Films and Multilayers.** Upon photoexcitation of a sample, a layer is generated at the surface where the optical constants are different than in the bulk. The degree of excitation decays exponentially as a function of distance into the sample, and the  $1/e$  point is known as the skin depth. This can lead to partial reflections and interference effects. A variety of issues relating to this phenomenon have been discussed in refs 49 and 50. This type of treatment must also be used when studying thin films on substrates.<sup>76</sup>

**D. Finite-Difference Time-Domain Numerical Propagation.** There are several situations when it is not appropriate to use Fourier transform methods to interpret the data. Two specific ones are (1) in TRTS studies at delay times near “ $t = 0$ ”, when the pump and probe pulses are traveling through the sample simultaneously, and (2) in the charge-transfer studies when the THz pulse is being generated as the visible pulse propagates through the medium.

In the first case, the optical constants of the medium are changing during the course of THz pulse propagation. This occurs when the response of the material changes rapidly compared to the time scale of the THz pulse electric field oscillations, typically on the sub-picosecond to few picosecond time scales. In these situations, it is meaningless to perform a Fourier transform of the transmitted pulse because different parts of the THz pulse have experienced a different absorption coefficient and refractive index as the medium changes. The solution to this problem is to scan synchronously and thereby “construct” a transmitted THz pulse in which every portion has experienced the same delay after the pump pulse, as discussed in previous publications.<sup>49,75</sup> Simulations using finite-difference time-domain (FDTD) method, wherein the pulse is propagated solely in the time-domain without ever Fourier transforming to the frequency-domain, have been indispensable in interpreting a variety of experimental situations. It is possible to describe the situation when the optical constants of the medium change *while* the THz pulse is traversing the sample with FDTD simulations.<sup>77</sup>

FDTD propagation is also necessary in the second case in which a THz pulse is generated as the visible pulse excites dye molecules in solution because the slowly varying envelope approximation (SVEA) is not valid for the THz pulse. Certainly, it is possible to describe electromagnetic pulse generation such

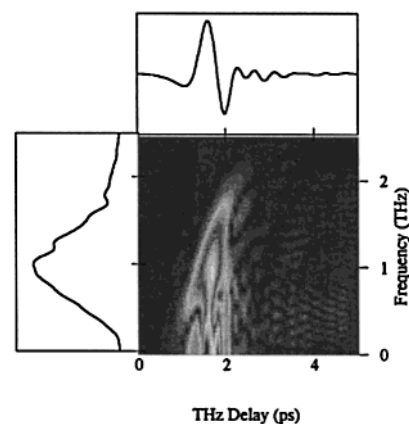


**Figure 3.** Wigner representation of a THz pulse. The horizontal axis corresponds to time, and the vertical axis corresponds to frequency. While the amplitude of a Wigner plot at a given point in time-frequency coordinates is not the intensity of a given frequency component at a particular time,<sup>98</sup> it does in fact represent the general progression of the frequency content as a function of time.

as lasing or even nonlinear phenomena when the generated pulse is well described by the SVEA. This is because both the excitation pulse and the generated pulse travel with a well-defined group velocity. Since the SVEA is not valid for the THz pulse generated, one must resort to FDTD methods.

**E. Wigner Representation.** Figure 3 is a Wigner representation of a THz pulse. While it is true that all the information is contained in the time-dependent electric field, a Wigner plot succinctly shows the evolution of the spectral components as a function of time. It is seen that the pulse is slightly chirped: that is, the higher frequency components arrive later than the lower frequency components. It must be noted that this does not adversely affect our temporal resolution because we scan the delay lines such that any given point in the analyzed THz waveform travels through the medium at the same amount of time after photoexcitation.

### III. Nontime-Resolved Studies

The first THz experiments carried out in our lab utilized the unamplified system and were not time-resolved.<sup>18,23</sup> The far-IR frequency-dependent absorption coefficient  $\alpha(\omega)$  and refractive index  $n(\omega)$  of neat liquids and binary mixtures were measured. This allows the complex-valued permittivity  $\epsilon(\omega)$  to be determined without invoking a Kramers–Kronig analysis. The permittivity is easily related to the susceptibility  $\chi(t)$ , which describes the response of a medium to an electric field and relates any optical experiment to the material being studied. Theoretical descriptions of liquid dynamics yield the frequency-dependent permittivity, so the experimental measurement of  $\epsilon(\omega)$ , or  $\chi(t)$  is essential for understanding liquid dynamics.

For example, the Debye model is the simplest description of liquid dynamics. It describes the molecular motion as rotational diffusion with a characteristic reorientational time constant  $\tau_D$ . Therefore, if the real and imaginary components of the permittivity display Debye-like behavior, then it is possible to attribute dynamical characteristics, i.e., reorientation time scales, to the liquid instead of simply reporting an absorption coefficient and index of refraction. We find Debye-like behavior for water, methanol, ethanol, and propanol, although a single Debye process is not sufficient to describe the measured data. Double-Debye or triple-Debye fits must be used instead.

Multiple-Debye fits are required when there are dynamics occurring on multiple time scales. In the case of water, there is

a very fast process with  $\tau_D \approx 180$  fs attributed to the breaking and formation of hydrogen bonds, and a slower process with  $\tau_D \approx 8.24$  ps attributed to molecular reorientation.<sup>18</sup> In the case of the small alcohols, there are actually three processes: hydrogen bond making and breaking with  $\tau_D \approx 200$  fs, end-of-chain molecular rotation about the hydrogen bond with  $\tau_D \approx 2$  ps, and molecular reorientation with  $\tau_D \approx 50$ –300 ps, depending on the molecule. The molecular reorientation time scale increases in going from methanol to propanol.<sup>18</sup>

We also studied binary mixtures of water with acetone, acetonitrile, and methanol in order to quantify the Debye relaxation dynamics in mixtures of highly polar liquids across the entire range of compositions.<sup>23,26</sup> We found that the absorption decreased and the reorientational time-constants increased considerably with compositions that were close to 50% water/50% nonaqueous, in a manner reminiscent of the changes observed when water is cooled.<sup>20,21</sup> Therefore, this was interpreted as an increase in the overall structure of the liquid at intermediate compositions.

Sometimes a great deal of information can be obtained by analyzing the results of MD simulations. In the far-IR region, the experimentally measured spectrum is often broad and featureless, so we have performed MD simulations of neat liquids and binary mixtures to attain deeper insight into liquid structure and dynamics.<sup>25,26</sup> If there is good agreement between the calculated far-IR spectrum and the measured spectrum, then one has an added level of confidence that the simulation is accurate and can be used for further understanding of the liquid or mixture.

Our initial foray into MD simulations was in the context of investigating whether instantaneous normal mode (INM) theory provided an accurate description of the far-IR spectrum of neat liquids.<sup>78</sup> Ultimately, our goal was to describe the solvent dynamics following photoexcitation of a dissolved dye molecule, and it was necessary to benchmark the methodology under equilibrium, or steady-state conditions. The reasoning was that INMs are a natural way to describe the *change* in the low-frequency intermolecular modes upon photoexcitation of a nearby solute molecule because the spectrum is obtained from a “snapshot” of the instantaneous configuration of the liquid at any given moment rather than the Fourier transform of the dipole–dipole time correlation function (TCF). This is particularly important when the solvent interactions are time-dependent, such as immediately after photoexcitation, because the TCF will depend on the point in time at which it begins.

More recently, our MD simulations have focused on the –OH librational band of water and methanol near  $670\text{ cm}^{-1}$  in a variety of binary mixtures.<sup>24–26</sup> As the fraction of water or methanol in a binary mixture with acetone or acetonitrile decreases, the librational band red-shifts by up to  $150\text{ cm}^{-1}$ . The MD simulations accurately reproduce this trend, and analysis of the MD results unambiguously attribute this trend to a loss of hydrogen bonding structure in the liquid upon dilution. As these were not THz studies, they are beyond the scope of this article and will not be discussed further.

#### IV. Time-Resolved Studies

We have spent considerable effort over the past few years characterizing and understanding TRTS,<sup>49</sup> and have now begun to apply it to novel systems. We have probed the collective low-frequency solvent response in a liquid when a dye molecule is photoexcited with an optical pulse.<sup>30</sup> We have measured the electromagnetic (EM) pulse emitted when a collection of dipolar molecules are partially oriented and coherently excited.<sup>69,70</sup> We

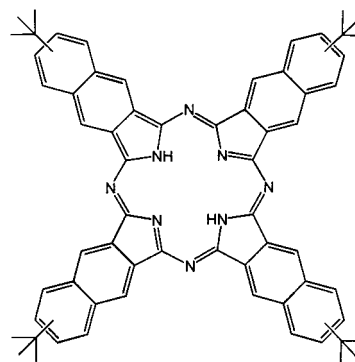


**Figure 4.** Structure of TBNC. Reprinted with permission from ref 30. Copyright 2002 American Chemical Society.

have determined the transient photoconductivity in materials such as LT-GaAs,<sup>50</sup> semiconductor quantum dots,<sup>79</sup> and sintered colloidal  $\text{TiO}_2$ ,<sup>76</sup> none of which can be characterized with conventional methods.

**A. Liquids.** Solvation and liquid dynamics play a very important role in essentially all liquid phase processes. Solvent effects are significant in photoexcitation, photoionization, electron transfer, proton transfer, energy dissipation, and liquid phase reactions. For example, the intermolecular solvent modes determine the ability of reactants to approach each other and products to separate from each other. Probing the low-frequency solvent modes directly while one of the above processes is proceeding is an effective method for understanding the solvent response to the event.<sup>28–30,80,81</sup>

A great deal has been learned about solvation and liquid dynamics through studies such as time-resolved fluorescence Stokes shift measurements wherein the solute's emission wavelength is monitored as a function of time after it has been photoexcited.<sup>82</sup> The emission red shifts as the surrounding solvent molecules reorient in response to the excited-state charge distribution and thereby solvate the excited state. While this type of experiment reveals the time scale of solvent reorganization, it does not provide direct information on the nature of the solvent dynamics that bring about solvation.

On the other hand, this information is accessible through TRTS experiments because the low-frequency collective intermolecular modes of a liquid absorb in the far-IR region of the spectrum. For example, we have studied the solvent dynamics of chloroform upon photoexcitation of TBNC (tetra-*tert*-butylnaphthalocyanine),<sup>30,80,81</sup> whose structure is shown in Figure 4. The 2D data set of difference scans (transmitted THz amplitude with excitation laser on vs laser off) is shown in Figure 5a. Because of group velocity mismatch between the visible and THz pulses, and the fact that the system is evolving on the time scale of the THz pulse, it is not correct to simply add the difference scan to a reference scan and perform a Fourier transform in order to obtain the frequency-dependent optical constants as a function of time after photoexcitation.<sup>49,50,75</sup> Instead, the response of the solvent must be modeled, and a simulation performed numerically and compared to the measured data. This is incorporated into a nonlinear least-squares fitting routine in which the parameters are iteratively adjusted until agreement with the experimental data is achieved. The results of the numerical propagation are shown in Figure 5b, and cuts at two different pump–probe delay times are shown in parts c and d in order to quantitatively judge the agreement of the simulation to the experimental data.

The process is modeled by treating the solvent as a collective damped, driven, harmonic oscillator (often referred to as a

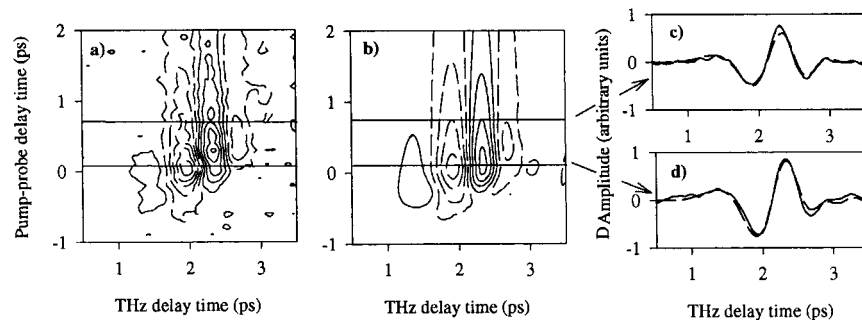


**Figure 5.** Contour plot of 2D TRTS difference signal (THz pulse propagated through sample with laser on minus that with laser off) for TBNC/chloroform. Solid contours correspond to positive values, and dashed contours are used for negative ones. Comparison of measured (part a), with calculated (part b) values. Parts c and d display two representative cuts through the surfaces as indicated by the horizontal lines in parts a and b. In parts c and d, the measured data are shown with solid lines, and results of the numerical propagation are shown with the dashed lines. Reprinted with permission from ref 30. Copyright 2002 American Chemical Society.

**TABLE 1: Lorentzian Oscillator Parameters for TBNC/Chloroform<sup>a</sup>**

oscillator #	$\eta_j$ (cm <sup>-1</sup> ) <sup>2</sup>	$\eta_j^*$ (cm <sup>-1</sup> ) <sup>2</sup>	$\omega_j$ (cm <sup>-1</sup> )	$\omega_j^*$ (cm <sup>-1</sup> )	$\gamma_j$ (cm <sup>-1</sup> )	$\gamma_j^*$ (cm <sup>-1</sup> )
1	171.4	1700(20)	41.60	97.9(0.1)	30.56	174.9(0.1)
2	115.3	180(5)	6.57	8.3(0.2)	19.35	29.5(0.1)
electronic		4.3(0.2)		2.4(0.1)		6.5(0.1)

#### Other Parameters

lifetime ( $\tau$ )	1.40(0.01) ps
visible pulse width ( $\Delta\omega$ )	150 fs (held fixed)
fraction excited ( $f_e$ )	0.05 (held fixed)
optical skin depth ( $\delta$ )	64 $\mu$ m (held fixed)

<sup>a</sup> Asterisks denote the photoexcited medium. The value of  $\eta_j$  reflects the strength of coupling of the oscillator to the field;  $\omega_j$  and  $\gamma_j$  are the resonant frequency and damping coefficient, respectively, of the oscillator. Other parameters used in the simulation are the lifetime of the excited state oscillators, the width of the excitation laser pulse, the fraction of oscillators excited, and the optical skin depth of the solution. See ref 30 for further details.

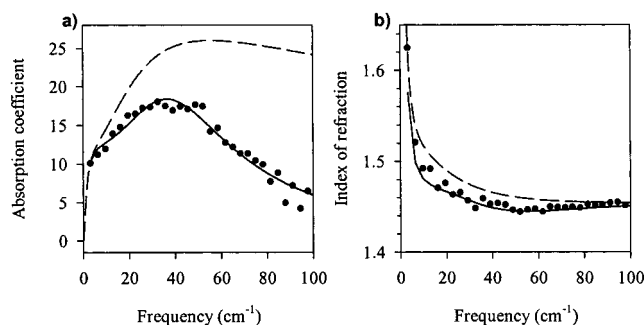


**Figure 6.** Frequency-dependent absorption coefficient and refractive index of  $\text{CHCl}_3$  under steady-state conditions (filled circles, and best fit solid line), and after photoexcitation of a nearby dye molecule (dashed line). It is seen that the mode centered at 42 cm<sup>-1</sup> becomes overdamped during the reorientation process. Reprinted with permission from ref 30. Copyright 2002 American Chemical Society.

multimode Brownian oscillator). The properties of the solvent in the absence of photoexcitation are obtained from its static far-IR spectrum. Since the solute concentration is about 10 mM, it is assumed that only a small fraction, on the order of 1%–5%, of the solvent is affected by photoexcitation of the dye molecules. After photoexcitation, the response has contributions from the static solvent, the “excited” solvent, and an instantaneous contribution that is present only while the photoexcitation pulse is in the medium, which is analogous to the coherent artifact of typical pump–probe studies. The “excited” solvent population decays away as a single exponential with a time constant of  $\sim 1$  ps as the molecules reorient around the photoexcited solvent and resume their usual dynamics.

Figure 6 displays the absorption coefficient and index of refraction for bulk  $\text{CHCl}_3$  (dots and solid line), and that for the small fraction of molecules that are near the photoexcited solute

molecules (dashed lines). The overall spectrum is essentially a linear combination of these two contributions whose coefficients depend on the amount of time elapsed since photoexcitation (and the instantaneous response, if appropriate). The parameters used in the simulation are given in Table 1. Chloroform is best described as having contributions from two damped, driven collective oscillators.<sup>83</sup> One is highly overdamped, resulting in nearly Debye-type behavior. The other is slightly underdamped, and is responsible for the peak at 42 cm<sup>-1</sup>. It is seen that upon photoexcitation, the Debye-like mode does not change, while the underdamped mode becomes overdamped, and its resonant frequency shifts to 175 cm<sup>-1</sup>. This behavior is interpreted as follows: Prior to excitation of the dye molecules, the solvent is undergoing librational motion. Upon photoexcitation, the nearby solvent molecules must reorient to the new charge distribution, and their librational motion becomes ill-defined, which is why the mode becomes overdamped. After a few picoseconds, they have reoriented and can resume their usual librational motion.

**B. Rapid ET.** Acceleration of charge generates EM radiation. From the mundane radio transmitter to the sophisticated synchrotron ring, the underlying principle is the same. In fact, the photoconductive antennas used in the unamplified THz setup described in section II are also governed by this same principle.

When a molecule undergoes intramolecular charge transfer, some fraction of an electron’s charge moves from one portion of the molecule to another, and therefore must undergo acceleration. Therefore, this process radiates an EM pulse. If the charge transfer occurs on a ps time scale, then the radiated pulse will fall in the THz region of the spectrum. If there is a random, isotropic distribution of photoexcited molecules, then the pulses emitted by each of the molecules will interfere destructively and no net signal will be measured. Also, if they



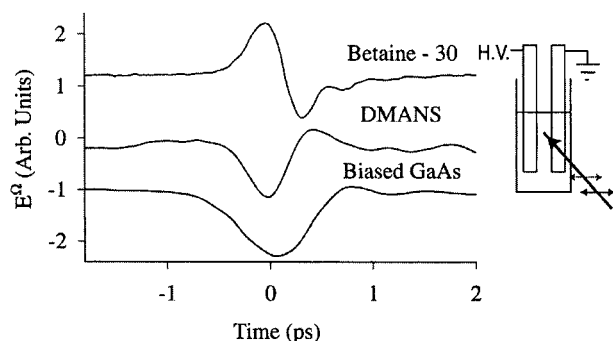


**Figure 7.** Electric fields generated via charge transfer in DMANS and Betaine-30 compared to that generated from photoexcitation of biased GaAs. The applied voltage is in the same direction for all three samples. A schematic representation of the cuvette and electrodes is shown to the right. Reprinted with permission from ref 69. Copyright 2002 American Chemical Society.

are excited continuously, then different molecules will radiate at different times, again leading to no net signal. However, if the molecules are oriented prior to photoexcitation, and are excited coherently with a short laser pulse, then the individual emissions will add together constructively resulting in a signal that can be measured.<sup>69,70</sup>

The direction of charge transfer determines the polarity of the emitted pulse. Since we detect the amplitude rather than the intensity of the THz pulse, we measure the direction of charge-transfer unambiguously. Furthermore, forward and back electron-transfer dynamics affect the precise shape of the emitted THz waveform if they are on a time scale of 0.1–10 ps. Figure 7 compares the EM pulse generated for two different dye molecules, Betaine-30 [2,6-diphenyl-4-(2,4,6-triphenylpyridinio)-phenolate], or Reichardt's dye, and DMANS (4-(dimethyl-amino)-4'-nitrostilbene). Structures of the dye molecules are shown in Figure 8, and the experimental apparatus is shown in Figure 9. In DMANS, charge transfer occurs in the same direction as its ground-state dipole, whereas in Betaine-30 charge transfer is in the opposite direction of its ground-state dipole. Therefore, the emitted pulses have opposite polarity. The emitted field is proportional to the difference between ground and excited-state dipoles multiplied by the ground-state dipole moment:  $(\mu_e - \mu_g) \cdot \mu_g$ . If the electron transfer time is much shorter than the solvent response time, then the measured dynamics will primarily reflect solvent reorganization. Table 2 summarizes the results for Betaine-30 and DMANS.<sup>69</sup>

**C. GaAs.** Grischkowsky and co-workers have shown that THz-TDS spectroscopy (the nontime-resolved variant) is capable of discerning subtle nuances in the frequency-dependent conductivity of lightly doped semiconductors<sup>44,45</sup> and conducting polymers,<sup>37</sup> but we are interested in the manner in which the conductivity of a sample *changes* upon photoexcitation. Our initial TRTS work characterized the transient photoconductivity of single crystal, undoped GaAs.<sup>49</sup> After the experimental

**TABLE 2: Optimized Parameters Resulting from Nonlinear Least-Squares Fits for Betaine-30 in Chloroform and DMANS in Toluene<sup>a</sup>**

	$\Delta w$ (fs)	$k_s$ (ps <sup>-1</sup> )	$\tau_s$ (fs)	$k_{ET}$ (ps <sup>-1</sup> )	$k_{BET}$ (ps <sup>-1</sup> )	$\tau_{BET}$ (ps)
betaine-30	150 <sup>b</sup>	2.86	350	>100 <sup>b</sup>	0.53	1.9
DMANS	150 <sup>b</sup>	1.37	730	>100 <sup>b</sup>	<0.01 <sup>b</sup>	>100 <sup>b</sup>

<sup>a</sup> The solvent response time constant is  $k_s$ ; the electron transfer and back electron transfer time constants are  $k_{ET}$  and  $k_{BET}$ , respectively. The corresponding time constants are included for convenience. The Gaussian width is given by  $\Delta w$ . <sup>b</sup> A value was held fixed during the fit.

apparatus was constructed and became operational, it became obvious that the methodology employed to determine the absorption coefficient  $\alpha(\omega)$  and refractive index  $n(\omega)$  in THz-TDS studies would not suffice when the sample's optical constants were changing as the THz pulse propagated through it. One of the primary motivations for carrying out the GaAs studies was that it would allow us to benchmark this new type of experiment, since GaAs is well understood based on work performed over the last 5 decades. A second motivation stemmed from a series of papers that predicted the time-resolved, frequency-dependent photoconductivity.<sup>84–88</sup> There were dramatic variations of the predicted complex-valued ac conductivity in the frequency range up to 3 THz, and the variations changed on a 300 fs time scale. Thus, the time and frequency ranges were perfectly suited for investigation with TRTS.

One important issue uncovered in the GaAs study was the requirement that the pump pulse spot size be larger than the THz probe spot size. This is true in any pump–probe experiment where it is desired that a uniformly excited medium be probed. It is particularly important in THz studies because of the broad range of wavelengths present in the bandwidth of the pulse: from 5 to 100 cm<sup>-1</sup>, corresponding to wavelengths of 2 mm to 100  $\mu$ m. The high-frequency components have a much smaller beam waist than the low-frequency components because the diffraction limit is on the order of  $\lambda/2$ . It is seen in Figure 10 that the measured change in far-IR optical density,  $\Delta OD$ , is skewed toward higher frequencies when the pump beam spot size is too small and only the high-frequency components of the THz pulse are significantly affected.

The band structure of GaAs and LT-GaAs is shown in Figure 11. The only difference between the two materials are the shallow defects and deep traps present in LT-GaAs that are absent in GaAs. The hole mobility is a factor of 7 less than the electron mobility, so the measured conductivity is attributed to electrons. The mobility in the L and X valleys is a factor of 10 lower than in the  $\Gamma$  valley,<sup>47</sup> so the THz absorption is dominated by electrons in the high-mobility  $\Gamma$  valley. Photoexcitation with 800 nm light leads to generation of carriers with only 115 meV excess kinetic energy above the bottom of the  $\Gamma$  valley, whereas photoexcitation with 400 nm light generates carriers with about

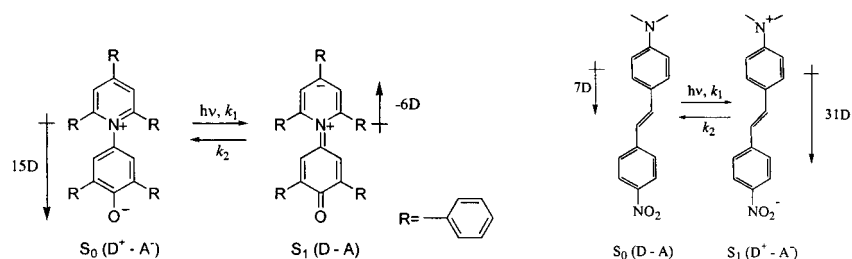


**Figure 8.** The ground,  $S_0$ , and first excited states,  $S_1$ , of Betaine-30 (left) and DMANS (right) and their respective dipole moments. Reprinted with permission from ref 69. Copyright 2002 American Chemical Society.

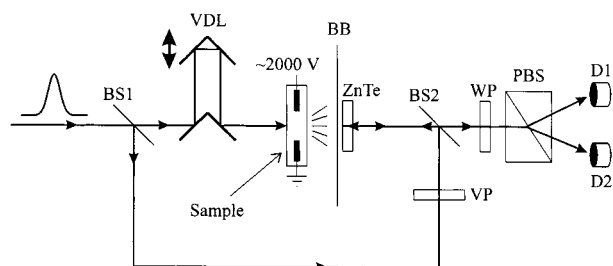


**Figure 9.** A more detailed experimental schematic of the set up used for rapid ET studies. An electrically biased solution is photoexcited to generate a THz pulse, which is then read out using free space electrooptic sampling in a ZnTe crystal.

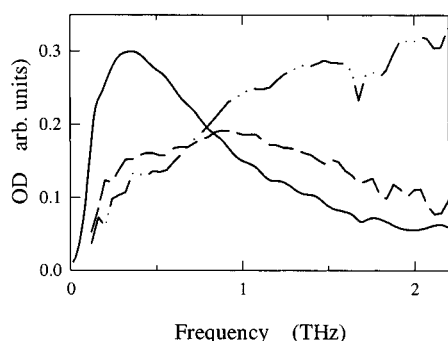


**Figure 10.** Change in optical density spectra of photoexcited GaAs as a function of visible (pump) spot size at 20 ps pump-probe delay time. The visible spot sizes are: 6.0 mm (solid line), 1.7 mm (dashed line), and 1.1 mm (dot-dashed line), whereas the THz spot size is 2.3 mm. The spectrum becomes skewed toward higher frequencies as the visible spot size becomes smaller than the THz spot size. The correct spectrum is obtained when the visible spot size is much larger than the THz probe spot size. Reprinted with permission from ref 49. Copyright 2000 American Physical Society.

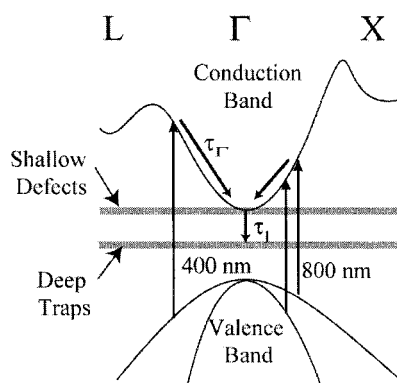


**Figure 11.** Band structure of GaAs and LT-GaAs. It is assumed that they are identical, except that LT-GaAs has shallow defects due to interstitials and lattice dislocations, as well as deep traps from the As clusters. Reprinted with permission from ref 50. Copyright 2001 American Institute of Physics.

1.6 eV kinetic energy allowing them to rapidly scatter into the low-mobility L and X valleys. It then takes several ps for the carriers to relax to the bottom of the high-mobility  $\Gamma$  valley. This behavior is illustrated in Figure 12, which is a 1D pump scan of the THz pulse amplitude at its highest point as a function of time after photoexcitation. The decrease in THz transmission is extremely rapid when exciting at 800 nm and much slower when exciting at 400 nm. Intermediate time scales are obtained when exciting with intermediate wavelengths.

We performed a series of 1D probe scans in which the full THz waveform is monitored 10–100 ps after the sample has been photoexcited. It is found that the Drude model, which is

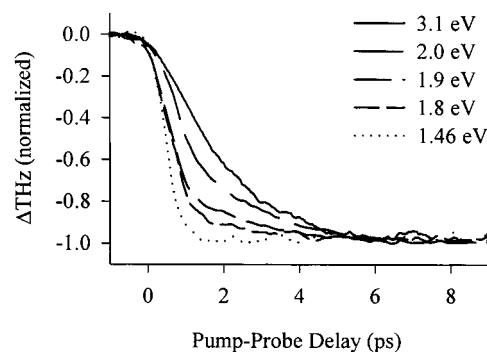


**Figure 12.** One-dimensional pump scans of GaAs(100) at different pump photon energies. At higher pump photon energies, photoexcited electrons can access the satellite valleys which have a lower mobility (see Figure 11). Since the absorption of THz radiation depends on the carrier mobility, the THz absorption will monitor the population in the  $\Gamma$  valley. Thus the onset of photoconductivity can be used to measure scattering rates from the satellite valley back to the central  $\Gamma$  valley. In going from the solid line to the dotted line, the excitation photon energy is 3.1, 2.0, 1.9, 1.8, and 1.55 eV. Reprinted with permission from ref 49. Copyright 2000 American Physical Society.

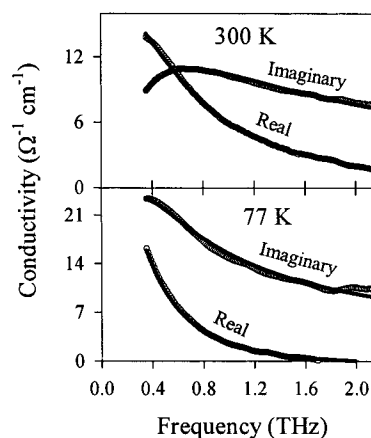


**Figure 13.** Best fits of measured conductivity in photoexcited GaAs at 77 and 300 K obtained about 100 ps after photoexcitation. It is seen that the generalized Drude (G-D) model is able to quantitatively describe the measured data. The differences between conductivity at 300 and 77 K arise from higher mobility at lower temperatures. Reprinted with permission from ref 49. Copyright 2000 American Physical Society.

the simplest model of conductivity, needs to be modified slightly to achieve quantitative agreement with the measured conductivity. The Drude model stipulates that the carriers scatter with an average scattering time  $\tau$  as they move through the sample, that the scattering is perfectly elastic, and that momentum is completely randomized upon scattering. It is mathematically equivalent to the Debye theory for liquids. It is found that the Drude model often must be modified in a fashion analogous to Cole–Cole or Cole–Davidson modifications for liquids in order to agree with measured data.<sup>44,49</sup> This type of modification allows for a distribution of scattering rates, rather than only a single scattering rate. We determine the carrier density and mobility based on this model. The carrier density extracted is in excellent agreement with that calculated based on knowledge of the pump beam intensity and spot size, and the optical skin depth of the sample. Figure 13 shows the measured frequency-dependent complex conductivity at 77 and 300 K, and compares it to that predicted from the generalized Drude model. It is worth stressing that the Fourier transform of a THz probe scan allows us to obtain the conductivity as a function of pump-delay time

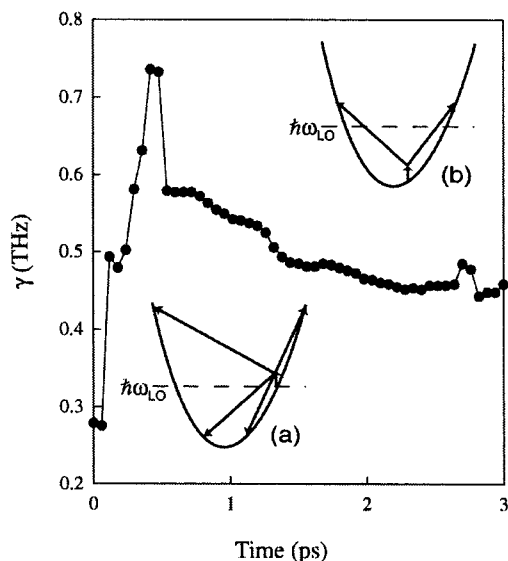


**Figure 14.** Plot of the frequency at the peak of the imaginary part of the conductivity as a function of time after photoexcitation. This value corresponds to the scattering rate,  $\gamma$ . Variations as a function of time are attributed to phonon-assisted intravalley relaxation. Inset a shows far-IR absorption assisted by LO phonon absorption and emission. Inset b shows that after the electron distribution has relaxed below  $\hbar\omega_{LO}$ , far-IR absorption is only assisted by LO phonon absorption. Reprinted with permission from ref 49. Copyright 2000 American Physical Society.

without assuming any model. If we choose, we can then compare the measured conductivity to a model calculation, as shown in Figure 13.

If dynamical information at the moment of photoexcitation is desired, then it is necessary to collect a 2D data set. We have discussed this at length in References 49, 50, and 75. In essence, a series of 1D probe scans are taken at a variety of pump delay times. This builds up a 2D data set where the frequency-dependent conductivity is determined at each of the pump delay times. Among other things, we can measure the time-dependent scattering rate as shown in Figure 14. This figure illustrates the utility of TRTS measurements: The electrical properties of a material are measured in a noncontact fashion with sub-ps temporal resolution. Initially the scattering rate is very low, which corresponds to ballistic transport, then the scattering rate increases to its maximum value at about 500 fs after photoexcitation. Finally, the scattering rate decreases and levels off on a 2 ps time scale as the carriers relax to the bottom of the  $\Gamma$  valley. This behavior is in the spirit of the Vengurlekar calculations,<sup>84–88</sup> but not in quantitative agreement.

**D. LT-GaAs.** The initial GaAs studies then led to a study of LT-GaAs.<sup>50</sup> This material has extremely fast carrier trapping rates, and is used in high-speed applications. It is impossible to characterize the mobility of photoexcited LT-GaAs using conventional techniques such as a four point probe because the material remains conductive for only  $\sim 2$ – $3$  ps after photoexcitation. Optical studies establish the time scale for the electron dynamics, but do not determine the mobility of the carriers prior to trapping. We are able to achieve this using TRTS.

The sample consists of a 0.5 mm thick wafer of regular undoped GaAs coated with a 50 nm thick barrier layer of  $\text{Al}_{0.6}\text{Ga}_{0.4}\text{As}$  followed by a  $1 \mu\text{m}$  thick layer of LT-GaAs. The LT-GaAs layer was annealed for 30 min at  $550^\circ\text{C}$  in an excess As flux. Because the material is grown and annealed in an excess As flux, there are initially many As antisites and interstitials. Annealing helps remove these but some shallow defects remain.

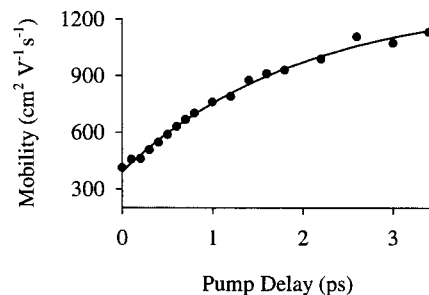


**Figure 15.** Time-dependent mobility of the carriers in LT-GaAs after photoexcitation at 400 nm. Reprinted with permission from ref 50. Copyright 2001 American Institute of Physics.

Thus, this material is not quite as good of a conductor as regular GaAs (which has a mobility of  $\sim 6540 \text{ cm}^2 \text{ V}^{-1} \text{ s}^{-1}$  at room temperature when the carrier density is  $1.6 \times 10^{16} \text{ cm}^{-3}$ ) even before the carriers become trapped. Deep traps are formed during the annealing phase when excess As atoms agglomerate into clusters. The properties of LT-GaAs are strongly influenced by the anneal time and temperature, because longer anneal times and/or higher temperatures lead to larger As clusters that are more widely separated.

The transient photoconductivity was characterized after photoexcitation with both 400 and 800 nm wavelengths. Photoexcitation at 400 nm produces carriers with sufficient kinetic energy to scatter into the L and X valleys, as already described for the photoexcitation of regular GaAs at 400 nm. The photoexcited carriers reside solely in the LT-GaAs layer because the absorption skin depth is only 14 nm. The measured photoconductivity is dominated by carriers that scatter back into the  $\Gamma$  valley and relax to the bottom, as illustrated for GaAs in Figure 12. Photoexcitation with 800 nm light generates carriers only at the bottom of the  $\Gamma$  valley. However, the optical skin depth is  $0.7 \mu\text{m}$  at this excitation wavelength, and therefore 23% of the incident photons penetrate the LT-GaAs layer and generate carriers in the GaAs substrate. Despite this fact, we are able to determine the mobilities in both the LT-GaAs and GaAs regions.<sup>50</sup>

Figure 15 displays the time-dependent mobility of the electrons after photoexcitation with 400 nm light. Data can only be obtained for  $\sim 3$  ps after photoexcitation because the carriers are trapped rapidly with a time constant of  $\sim 1.1$  ps. It is seen that the mobility increases from 400 to  $1200 \text{ cm}^2 \text{ V}^{-1} \text{ s}^{-1}$  as the carriers scatter back and relax in the  $\Gamma$  valley. When exciting close to the bottom of the  $\Gamma$  valley with 800 nm light, the mobility remains constant at  $3000 \text{ cm}^2 \text{ V}^{-1} \text{ s}^{-1}$  (not shown). This level of detail simply could not be attained with any other experimental technique.

**E. Transient Photoconductivity in Colloidal Sintered  $\text{TiO}_2$  and CdSe Quantum Dots.** The final two topics, colloidal sintered  $\text{TiO}_2$  and quantum dots, represent studies under current investigation. That is, the results presented here provide only a glimpse of what is to come. These systems have generated a great deal of interest among researchers in many fields, and we feel that since TRTS is a noncontact electrical probe with subpicosecond temporal resolution, we can make unique and important contributions to the understanding of these novel materials.

*i.  $\text{TiO}_2$ .* Colloidal sintered  $\text{TiO}_2$  forms the heart of the so-called “Grätzel cell”, a dye-sensitized solar cell that has attracted attention since 1991.<sup>89</sup> A schematic of dye sensitization of  $\text{TiO}_2$  is shown in Figure 16. The general idea is that even though the photon energy may not be great enough to excite an electron from the valence to conduction band in the bulk, carriers can

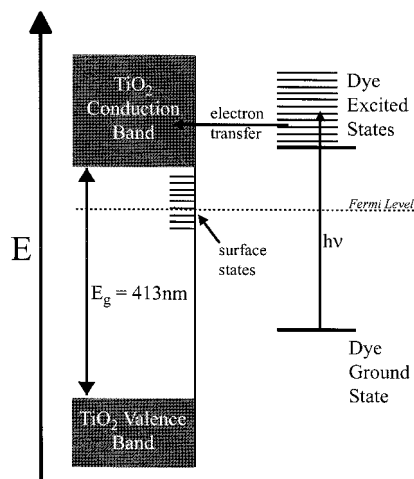


**Figure 16.** Schematic of dye sensitization of TiO<sub>2</sub>. The dye molecule absorbs a photon and injects an electron into the TiO<sub>2</sub> conduction band.

still be generated by photoexciting a dye molecule on the surface which then injects an electron into the semiconductor. Most of the ultrafast spectroscopy done on this system has focused on the dye molecule. That is, a sharp reduction in fluorescence quantum yield and lifetime is observed when the molecule is adsorbed to TiO<sub>2</sub> compared to when it is in solution, and is attributed to rapid electron injection upon photoexcitation.

Our desire is to characterize the photoinjected electron dynamics following excitation by monitoring the transient THz absorption.<sup>76</sup> The only other closely related studies were carried out in the mid-IR region of the spectrum.<sup>90,91</sup> While those studies provide some measure of carrier dynamics, they must assume Drude-like behavior of the electrons because they attribute the transient IR absorption to free carrier absorption (FCA) by the electrons. This assumption need not be made in our studies because we measure the frequency-dependent complex conductivity, and the far-IR region of the spectrum is very sensitive to scattering rates in this type of system. In particular, for a Drude conductor the imaginary component of the frequency-dependent conductivity has its maximum value at the radial frequency that corresponds to the scattering rate. Since scattering times  $\tau_s$  are often on the order of 10 to 100 fs, the imaginary conductivity peaks at  $f_{\text{peak}}$  of 16 THz to 1.6 THz [ $f_{\text{peak}} = 1/(2\pi\tau_s)$ ]. Even if the carriers do not behave in a Drude-like manner, the complex conductivity will still have large variations in the far-IR region of the spectrum. We obtain the complex conductivity without assuming any model whatsoever. This allows a deeper level of understanding of the carrier dynamics because Drude-like behavior may be uncovered, as in the case of GaAs or LT-GaAs. On the other hand, it may be that the data obtained are fundamentally and qualitatively non-Drude-like, as in the case of TiO<sub>2</sub>.

The TiO<sub>2</sub> samples are dry thin films roughly 5  $\mu\text{m}$  thick. They are created by spin coating a solution of  $\sim 25$  nm diameter nanocrystalline TiO<sub>2</sub> particles (Degussa P25, 70% anatase, and 30% rutile) onto a quartz substrate, annealing at 500  $^{\circ}\text{C}$  for 30 min, and staining with a dye solution for 1 to 10 h. We have employed two different dyes (Coumarin 343 and Ruthenium 535) as well as photoexciting nonsensitized colloidal TiO<sub>2</sub> (not shown), to verify that the subsequent dynamics are independent of the manner in which the carriers arrive in the conduction band, as would be expected, and is shown in Figure 17. There is a transient on a 20 ps time scale that is present in the dye-sensitized samples which is absent in the nonsensitized sample, however. The origin of this feature is under current investigation,

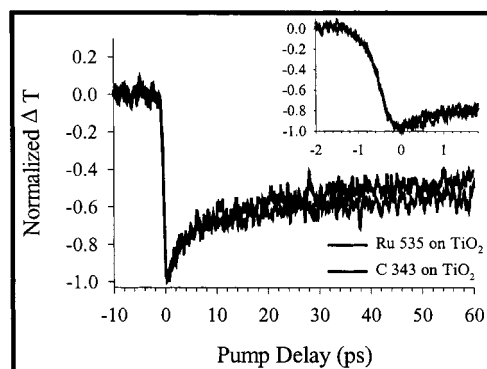


**Figure 17.** Comparison of pump-probe dynamics for two different dyes (Ru535 and C343). It is seen that the response is essentially independent of dye. The inset displays the onset of absorption on an expanded time scale.

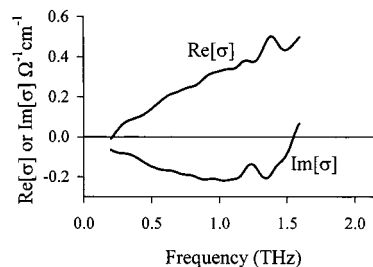


**Figure 18.** Real and imaginary components of complex conductivity in colloidal TiO<sub>2</sub>. Note that the imaginary component is negative.

and might be due to differences in surface pH. More importantly, the overall signal strength is enhanced by a factor of 5–10 when exciting the dye-sensitized samples relative to the bare ones. This occurs because the 400 nm wavelength of the excitation photons is roughly equal to the band gap of the material, but the band edge is not very sharp. Therefore, there is some carrier generation in the nonsensitized material, but not very much.

One of the most significant results of this work is that the carriers behave in a highly non-Drude manner in colloidal, sintered TiO<sub>2</sub>. Figure 18 displays the measured real and imaginary components of the frequency-dependent conductivity roughly 50 ps after photoexcitation. This behavior is understood through the modification to the Drude model developed by Smith.<sup>92</sup> The unique aspect Smith's modification of the Drude model is including a "persistence of velocity" parameter. One of the basic tenets of the Drude model is that the momentum of the carrier is completely randomized after every collision. Smith's generalization allows for a memory of the velocity prior to scattering to influence its velocity after scattering. For elastic collisions, the parameter  $c$  can be interpreted as the expectation value of  $\cos\theta$ ,  $\langle\cos\theta\rangle$ , where  $\theta$  is the scattering angle. There are indeed other modifications, or generalizations, of the Drude model,<sup>44,49</sup> but they do not allow for a negative imaginary component of the conductivity.

*ii. Quantum Dots.* Semiconductor quantum dots (QDs) have received considerable attention over the past decade. The prototypical material has been CdSe, but a wide variety of II–VI and III–V materials have been investigated, as well as Si, and Ge (group IV). There has also been a great deal of work studying metallic nanoparticles such as Ag, Au, Pb, etc.

One of the most important type of study involving quantum dots is the determination of how a particular property varies as a function of particle size. By far, the optical band gap has been the most probed property of semiconductor QDs, although trends in melting temperature, lattice constant, and other properties

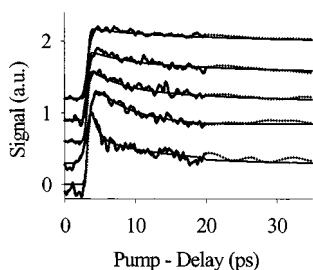


**Figure 19.** One-dimensional pump delay scans of CdSe quantum dots of various sizes. In going from top to bottom, the particle diameters are >25, 15, 10, and 4.1 nm, along with quantum rods of  $\sim 3$  nm diameter. Smooth curves are triple-exponential fits. It is seen that smaller particles have a rapidly decaying component in the signal, which is attributed to surface trapping.

have also been determined for one or more materials. The basic goal of our work is to determine the size-dependence of the “photoconductivity”.<sup>79</sup>

Certainly, in large enough particles, the photoconductivity will be identical to that in bulk, and in very small particles it will be nonexistent because there is not enough room for the carriers to move. There should still be a small amount of THz absorption by small QDs upon photoexcitation, but that is due to the fact that the electron–hole pair is polarizable rather than mobile. In any case, the ability to characterize the time-resolved, frequency-dependent photoconductivity without attaching wires to the sample will allow us to characterize the size-dependent properties of semiconductor QDs.

We have synthesized CdSe, CdS, and CdTe particles using the method described in ref 93, and have characterized their size and uniformity with transmission electron microscopy, absorption spectroscopy, and luminescence spectroscopy. Figure 19 shows pump-delay scans of several sizes of CdSe QDs. It is seen that the response is strongly size-dependent. The fast component in the multiexponential decay is much more pronounced in the smaller particles, which have higher surface-to-volume ratios. Figure 20 shows probe delay scans of the same samples taken a few ps after photoexcitation, and it is clear that there is a large change in phase delay (which is related to the refractive index of the sample) upon photoexcitation. It is seen that  $\Delta OD$  is small for all particle sizes, and there is a large variation in  $\Delta\phi$  as a function of size. Furthermore, the transient responses cluster into three groups, but further analysis is required to understand this behavior.

## V. Future Work

As discussed in the Introduction section, there are many interesting and powerful attributes of THz spectroscopy. We will continue to pursue *time-resolved* THz spectroscopy because

this aspect of THz spectroscopy is truly unique in that there simply does not exist any other way to generate subpicosecond far-IR pulses. Extensions of the work described in sections IV.B and IV.E will constitute the focus of near-term future studies.

The approach used in the ET studies will be applied to thin films and self-assembled monolayers, and ultimately to bacterial reaction centers (RCs). The *Rhodobacter sphaeroides* RC absorbs strongly at 800 nm, and incorporates a charge transfer over a distance of 17 Å in 2.3 ps. There is still uncertainty whether the charge-transfer involves a hopping mechanism incorporating the intervening chlorophyll, or if it is a one step process mediated by superexchange, which is quantum mechanical tunneling through the intervening chlorophyll.

The initial transient photoconductivity studies of sintered colloidal TiO<sub>2</sub> will be followed up with a full investigation of temperature and size dependence, which will lead to a better understanding of the mechanism behind the conductivity in this material. Future work will include comparisons with other materials, such as SnO<sub>2</sub> and ZnO, as well as steps toward probing these materials under conditions that are found in working devices.

The initial transient photoconductivity studies of QDs discussed in this article will be rounded out with a full investigation of size, temperature, and capping layer dependence. Future work will address the role of coupling in QD solids. One expects a sharp change in the far-IR optical constants when the particles in the QD solid are close enough together for coupling to occur.

In a more global sense, the future of THz spectroscopy includes the following areas: Two- and three-dimensional imaging of biological and nonbiological media,<sup>33,94</sup> line resolved THz spectroscopy, and nonlinear THz spectroscopy. Imaging of biological media in vivo will suffer from the problem of water absorption, although there are situations where it will not pose a problem, such as reflection spectroscopy off skin, and transmission spectroscopy through teeth and fatty tissue. For other tissues, it will be necessary to fix them in paraffin, as is presently done for other assays.

As already mentioned, another very active area of THz spectroscopy will be time-resolved THz spectroscopy involving an optical pump pulse. Fundamental advances in the understanding of essential processes in semiconductors, superconductors, magnetic media, liquids, and biological media will all be achieved. This will open new vistas in physical chemistry in the same fashion as have time-resolved spectroscopy in the visible, IR, and UV regions of the spectrum.

Finally, nonlinear experiments involving only THz pulses will emerge, that is, THz pump/THz probe spectroscopy and 2-dimensional THz spectroscopy. For example, this will allow intermolecular couplings in liquids to be monitored in a fashion

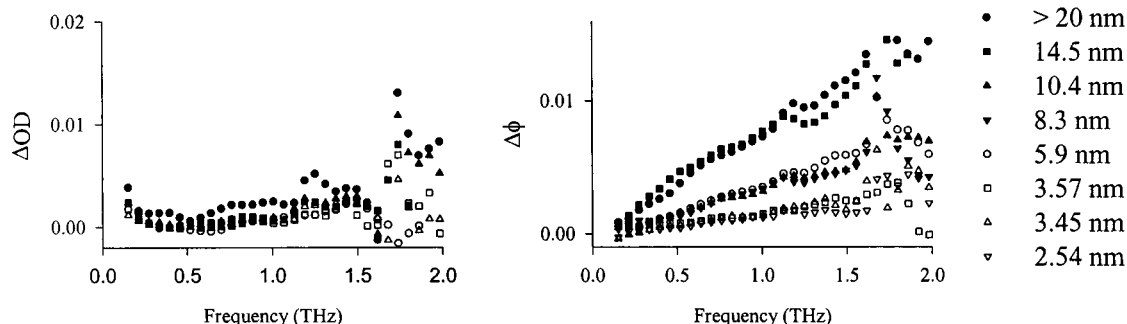


**Figure 20.** One-dimensional probe delay scans of CdSe quantum dots of various sizes. Change in frequency-dependent optical density and phase for eight sizes of CdSe QDs. The  $\Delta OD$  is small and more or less constant, and the  $\Delta\phi$  varies with size, and clusters into three groups. We are currently trying to understand this clustering behavior.

similar to intramolecular or electronic couplings measured in 2-dimensional IR<sup>95,96</sup> and optical spectroscopies,<sup>97</sup> respectively, which are analogous in many respects to 2-d NMR experiments. The ability to easily characterize and control the phase of the THz pulses will be a distinct advantage.

## VI. Summary and Conclusions

The field of THz spectroscopy continues to steadily gain momentum. Now that technical issues related to source and detector development have been worked out, this methodology can be treated as yet another weapon in the physical chemist's arsenal. This article has provided a glimpse of the tremendous variety of studies carried out under the broad heading of THz spectroscopy. Certainly, the broadband far-IR coverage makes it a convenient and sensitive technique, but many workers find that exploiting one or more of its unique characteristics leads to more valuable information.

The fact that the time-dependent amplitude of the pulse, as opposed to its intensity, is measured allows the full complex-valued generalized permittivity to be obtained without invoking a Kramers–Kronig analysis. The fact that the peak amplitude is roughly 1000–10000 times greater than the baseline fluctuations, implies power absorption detection levels on the order of 1 part in 10<sup>5</sup>, and potentially on the order of 1 part in 10<sup>8</sup>. Finally, the fact that time-resolved studies on a sub-ps time scale can now be carried out in the far-IR region of the spectrum has allowed a variety of interesting systems to be studied. For example, the low-frequency response of collective solvent modes in liquids, or the transient conductivity of novel nanoscale materials can now be probed in a very direct manner. The future of THz spectroscopy is a bright one.

**Acknowledgment.** This work has been funded over the years from the Petroleum Research Fund (type G) administered by the American Chemical Society, the Dreyfus Foundation (New Faculty Award), the National Science Foundation Division of Chemistry (CAREER Award), and the Sloan Foundation. We also thank Dr. James Kindt and Dr. Dean Venables for their contributions to these projects.

## References and Notes

- Smith, P. R.; Auston, D. H.; Nuss, M. C. *IEEE J. Quantum Electron.* **1988**, *24*, 255–260.
- Fattinger, C.; Grischkowsky, D. *Appl. Phys. Lett.* **1989**, *54*, 490–492.
- Siegel, P. H. *IEEE Trans. Microwave Theory Tech.* **2002**, *50*, 910–928.
- Harde, H.; Chevillon, R. A.; Grischkowsky, D. *J. Opt. Soc. Am. B: Opt. Phys.* **1997**, *14*, 3282–3293.
- Chevillon, R. A.; Grischkowsky, D. *J. Opt. Soc. Am. B: Opt. Phys.* **1999**, *16*, 317–322.
- Chevillon, R. A.; Grischkowsky, D. *Opt. Lett.* **1998**, *23*, 531–533.
- Lipkin, R. *Sci. News* **1995**, *148*, 136–137.
- Hu, B. B.; Nuss, M. C. *Opt. Lett.* **1995**, *20*, 1716–&.
- Hunsche, S.; Mittleman, D. M.; Koch, M.; Nuss, M. C. *IEICE Trans. Electron.* **1998**, *E81C*, 269–276.
- Mickan, S.; Abbott, D.; Munch, J.; Zhang, X. C.; van Doorn, T. *Microelectron. J.* **2000**, *31*, 503–514.
- Mittleman, D. M.; Cunningham, J.; Nuss, M. C.; Geva, M. *Appl. Phys. Lett.* **1997**, *71*, 16–18.
- Jiang, Z. P.; Zhang, X. C. *IEEE Trans. Microwave Theory Tech.* **1999**, *47*, 2644–2650.
- Chevillon, R. A.; McGowan, R. W.; Grischkowsky, D. *Phys. Rev. Lett.* **1998**, *80*, 269–272.
- Chevillon, R. A.; Grischkowsky, D. *Appl. Phys. Lett.* **1995**, *67*, 1960–1962.
- Mittleman, D. M.; Hunsche, S.; Boivin, L.; Nuss, M. C. *Opt. Lett.* **1997**, *22*, 904–906.
- Mittleman, D. M.; Gupta, M.; Neelamani, R.; Baraniuk, R. G.; Rudd, J. V.; Koch, M. *Appl. Phys. B: Lasers Opt.* **1999**, *68*, 1085–1094.
- Keiding, S. R. *J. Phys. Chem. A* **1997**, *101*, 5250–5254.
- Kindt, J. T.; Schmuttenmaer, C. A. *J. Phys. Chem.* **1996**, *100*, 10373–10379.
- Nymand, T. M.; Rønne, C.; Keiding, S. R. *J. Chem. Phys.* **2001**, *114*, 5246–5255.
- Rønne, C.; Thrane, L.; Astrand, P. O.; Wallqvist, A.; Mikkelsen, K. V.; Keiding, S. R. *J. Chem. Phys.* **1997**, *107*, 5319–5331.
- Rønne, C.; Astrand, P. O.; Keiding, S. R. *Phys. Rev. Lett.* **1999**, *82*, 2888–2891.
- Rønne, C.; Jensby, K.; Loughnane, B. J.; Fourkas, J.; Nielsen, O. F.; Keiding, S. R. *J. Chem. Phys.* **2000**, *113*, 3749–3756.
- Venables, D. S.; Schmuttenmaer, C. A. *J. Chem. Phys.* **1998**, *108*, 4935–4944.
- Venables, D. S.; Chiu, A.; Schmuttenmaer, C. A. *J. Chem. Phys.* **2000**, *113*, 3243–3248.
- Venables, D. S.; Schmuttenmaer, C. A. *J. Chem. Phys.* **2000**, *113*, 3249–3260.
- Venables, D. S.; Schmuttenmaer, C. A. *J. Chem. Phys.* **2000**, *113*, 11222–11236.
- Thrane, L.; Jacobsen, R. H.; Jepsen, P. U.; Keiding, S. R. *Chem. Phys. Lett.* **1995**, *240*, 330–333.
- Haran, G.; Sun, W. D.; Wynne, K.; Hochstrasser, R. M. *Chem. Phys. Lett.* **1997**, *274*, 365–371.
- McElroy, R.; Wynne, K. *Phys. Rev. Lett.* **1997**, *79*, 3078–3081.
- Beard, M. C.; Turner, G. M.; Schmuttenmaer, C. A. *Low Frequency, Collective Solvent Dynamics Probed with Time-Resolved THz Spectroscopy. In Liquid Dynamics: Experiment, Simulation, and Theory*; Fourkas, J. T., Ed.; American Chemical Society: Washington, DC, 2002; pp 44–57.
- Knoesel, E.; Bonn, M.; Shan, J.; Heinz, T. F. *Phys. Rev. Lett.* **2001**, *86*, 340–343.
- Cook, D. J.; Chen, J. X.; Morlino, E. A.; Hochstrasser, R. M. *Chem. Phys. Lett.* **1999**, *309*, 221–228.
- Han, P. Y.; Cho, G. C.; Zhang, X. C. *Opt. Lett.* **2000**, *25*, 242–244.
- Markelz, A. G.; Roitberg, A.; Heilweil, E. J. *Chem. Phys. Lett.* **2000**, *320*, 42–48.
- Walther, M.; Fischer, B.; Schall, M.; Helm, H.; Jepsen, P. U. *Chem. Phys. Lett.* **2000**, *332*, 389–395.
- Brucherseifer, M.; Nagel, M.; Bolivar, P. H.; Kurz, H.; Bosserhoff, A.; Buttner, R. *Appl. Phys. Lett.* **2000**, *77*, 4049–4051.
- Jeon, T. I.; Grischkowsky, D.; Mukherjee, A. K.; Menon, R. *Appl. Phys. Lett.* **2000**, *77*, 2452–2454.
- Grischkowsky, D.; Keiding, S.; Vanexter, M.; Fattinger, C. *J. Opt. Soc. Am. B: Opt. Phys.* **1990**, *7*, 2006–2015.
- Zhang, C.; Lee, K. S.; Zhang, X. C.; Wei, X.; Shen, Y. R. *Appl. Phys. Lett.* **2001**, *79*, 491–493.
- Li, M.; Fortin, J.; Kim, J. Y.; Fox, G.; Chu, F.; Davenport, T.; Lu, T. M.; Zhang, X. C. *IEEE J. Sel. Top. Quantum Electron.* **2001**, *7*, 624–629.
- Grischkowsky, D.; Keiding, S. *Appl. Phys. Lett.* **1990**, *57*, 1055–1057.
- Averitt, R. D.; Lobad, A. I.; Kwon, C.; Trugman, S. A.; Thorsmolle, V. K.; Taylor, A. J. *Phys. Rev. Lett.* **2001**, *8701* (article no. 017401).
- Averitt, R. D.; Rodriguez, G.; Lobad, A. I.; Siders, J. L. W.; Trugman, S. A.; Taylor, A. J. *Phys. Rev. B* **2001**, *6314* (article no. 140502).
- Jeon, T. I.; Grischkowsky, D. *Appl. Phys. Lett.* **1998**, *72*, 2259–2261.
- Jeon, T. I.; Grischkowsky, D. *Phys. Rev. Lett.* **1997**, *78*, 1106–1109.
- Jepsen, P. U.; Schairer, W.; Libon, I. H.; Lemmer, U.; Hecker, N. E.; Birkholz, M.; Lips, K.; Schall, M. *Appl. Phys. Lett.* **2001**, *79*, 1291–1293.
- Nuss, M. C.; Auston, D. H.; Capasso, F. *Phys. Rev. Lett.* **1987**, *58*, 2355–2358.
- Schall, M.; Jepsen, P. U. *Opt. Lett.* **2000**, *25*, 13–15.
- Beard, M. C.; Turner, G. M.; Schmuttenmaer, C. A. *Phys. Rev. B* **2000**, *62*, 15764–15777.
- Beard, M. C.; Turner, G. M.; Schmuttenmaer, C. A. *J. Appl. Phys.* **2001**, *90*, 5915–5923.
- Huber, R.; Tausser, F.; Brodschelm, A.; Bichler, M.; Abstreiter, G.; Leitenstorfer, A. *Nature* **2001**, *414*, 286–289.
- Cho, G. C.; Han, P. Y.; Zhang, X. C.; Bakker, H. J. *Opt. Lett.* **2000**, *25*, 1609–1611.
- Schall, M.; Jepsen, P. U. *Appl. Phys. Lett.* **2000**, *77*, 2801–2803.
- Schall, M.; Walther, M.; Jepsen, P. U. *Phys. Rev. B* **2001**, *6409* (article no. 094301).
- van Exter, M.; Grischkowsky, D. R. *IEEE Trans. Microwave Theory Tech.* **1990**, *38*, 1684–1691.
- Wu, Q.; Litz, M.; Zhang, X. C. *Appl. Phys. Lett.* **1996**, *68*, 2924–2926.
- Brener, I.; Dykaar, D.; Frommer, A.; Pfeiffer, L. N.; Lopata, J.; Wynn, J.; West, K.; Nuss, M. C. *Opt. Lett.* **1996**, *21*, 1924–1926.

- (58) Huber, R.; Brodschelm, A.; Tauser, F.; Leitenstorfer, A. *Appl. Phys. Lett.* **2000**, *76*, 3191–3193.
- (59) Wu, Q.; Zhang, X. C. *Appl. Phys. Lett.* **1997**, *71*, 1285–1286.
- (60) Jacobsen, R. H.; Birkelund, K.; Holst, T.; Jepsen, P. U.; Keiding, S. R. *J. Appl. Phys.* **1996**, *79*, 2649–2657.
- (61) Jepsen, P. U.; Jacobsen, R. H.; Keiding, S. R. *J. Opt. Soc. Am. B: Opt. Phys.* **1996**, *13*, 2424–2436.
- (62) Nemeč, H.; Pashkin, A.; Kuzel, P.; Khazan, M.; Schnull, S.; Wilke, I. *J. Appl. Phys.* **2001**, *90*, 1303–1306.
- (63) Brener, I.; Planken, P. C. M.; Nuss, M. C.; Luo, M. S. C.; Chuang, S. L.; Pfeiffer, L.; Leaird, D. E.; Weiner, A. M. *J. Opt. Soc. Am. B: Opt. Phys.* **1994**, *11*, 2457–2469.
- (64) Leitenstorfer, A.; Hunsche, S.; Shah, J.; Nuss, M. C.; Knox, W. H. *Phys. Rev. B* **2000**, *61*, 16642–16652.
- (65) Leitenstorfer, A.; Hunsche, S.; Shah, J.; Nuss, M. C.; Knox, W. H. *Phys. B* **1999**, *272*, 348–352.
- (66) Leitenstorfer, A.; Hunsche, S.; Shah, J.; Nuss, M. C.; Knox, W. H. *Phys. Rev. Lett.* **1999**, *82*, 5140–5143.
- (67) Markelz, A. G.; Heilweil, E. J. *Appl. Phys. Lett.* **1998**, *72*, 2229–2231.
- (68) Sarukura, N.; Ohtake, H.; Izumida, S.; Liu, Z. L. *J. Appl. Phys.* **1998**, *84*, 654–656.
- (69) Beard, M. C.; Turner, G. M.; Schmittenmaer, C. A. *J. Phys. Chem. A* **2002**, *106*, 878–883.
- (70) Beard, M. C.; Turner, G. M.; Schmittenmaer, C. A. *J. Am. Chem. Soc.* **2000**, *122*, 11541–11542.
- (71) Rice, A.; Jin, Y.; Ma, X. F.; Zhang, X. C.; Bliss, D.; Larkin, J.; Alexander, M. *Appl. Phys. Lett.* **1994**, *64*, 1324–1326.
- (72) Nahata, A.; Weling, A. S.; Heinz, T. F. *Appl. Phys. Lett.* **1996**, *69*, 2321–2323.
- (73) Cai, Y.; Brener, I.; Lopata, J.; Wynn, J.; Pfeiffer, L.; Stark, J. B.; Wu, Q.; Zhang, X. C.; Federici, J. F. *Appl. Phys. Lett.* **1998**, *73*, 444–446.
- (74) Winnewisser, C.; Jepsen, P. U.; Schall, M.; Schyja, V.; Helm, H. *Appl. Phys. Lett.* **1997**, *70*, 3069–3071.
- (75) Kindt, J. T.; Schmittenmaer, C. A. *J. Chem. Phys.* **1999**, *110*, 8589–8596.
- (76) Turner, G. M.; Beard, M. C.; Schmittenmaer, C. A. *J. Phys. Chem. B* **2002**, Submitted for publication.
- (77) Beard, M. C.; Schmittenmaer, C. A. *J. Chem. Phys.* **2001**, *114*, 2903–2909.
- (78) Kindt, J. T.; Schmittenmaer, C. A. *J. Chem. Phys.* **1997**, *106*, 4389–4400.
- (79) Beard, M. C.; Turner, G. M.; Schmittenmaer, C. A. *Nano Lett.* **2002**, Submitted.
- (80) Turner, G. M.; Beard, M. C.; Venables, D. S.; Schmittenmaer, C. A. In *Tenth Annual Symposium on Photoinduced Charge Transfer*; World Scientific: NJ, 2000; pp 223–232.
- (81) Beard, M. C.; Turner, G. M.; Schmittenmaer, C. A. In *Ultrafast Phenomena XIII; Springer Series on Chemical Physics*; Springer: New York, 2001; Vol. 66, pp 522–524.
- (82) Castner, E. W.; Maroncelli, M. *J. Mol. Liq.* **1998**, *77*, 1–36.
- (83) Gerschel, A.; Darmon, I.; Brot, C. *Mol. Phys.* **1972**, *23*, 317–&.
- (84) Vengurlekar, A. S.; Jha, S. S. *Appl. Phys. Lett.* **1987**, *51*, 323–325.
- (85) Vengurlekar, A. S.; Jha, S. S. *Phys. Rev. B: Condens. Matter* **1988**, *38*, 2044–2056.
- (86) Vengurlekar, A. S.; Jha, S. S. *J. Appl. Phys.* **1989**, *65*, 3189–3196.
- (87) Vengurlekar, A. S.; Jha, S. S. *Phys. Rev. B: Condens. Matter* **1990**, *41*, 1286–1289.
- (88) Vengurlekar, A. S.; Jha, S. S. *Phys. Rev. B: Condens. Matter* **1991**, *43*, 12454–12457.
- (89) O'Regan, B.; Gratzel, M. *Nature* **1991**, *353*, 737–740.
- (90) Ghosh, H. N.; Asbury, J. B.; Lian, T. Q. *J. Phys. Chem. B* **1998**, *102*, 6482–6486.
- (91) Heimer, T. A.; Heilweil, E. J. *J. Phys. Chem. B* **1997**, *101*, 10990–10993.
- (92) Smith, N. V. *Phys. Rev. B* **2001**, *6415*, 5106.
- (93) Peng, Z. A.; Peng, X. G. *J. Am. Chem. Soc.* **2001**, *123*, 183–184.
- (94) Smye, S. W.; Chamberlain, J. M.; Fitzgerald, A. J.; Berry, E. *Phys. Med. Biol.* **2001**, *46*, R101–R112.
- (95) Asplund, M. C.; Zanni, M. T.; Hochstrasser, R. M. *Proc. Nat. Acad. Sci. U.S.A.* **2000**, *97*, 8219–8224.
- (96) Golonzka, O.; Khalil, M.; Demirdoven, N.; Tokmakoff, A. *Phys. Rev. Lett.* **2001**, *86*, 2154–2157.
- (97) Hybl, J. D.; Albrecht, A. W.; Faeder, S. M. G.; Jonas, D. M. *Chem. Phys. Lett.* **1998**, *297*, 307–313.
- (98) Paye, J. *IEEE J. Quantum Electron.* **1992**, *28*, 2262–2273.